nature portfolio

https://doi.org/10.1038/s41560-022-01013-w

Supplementary information

Cost and potential of metal–organic frameworks for hydrogen back-up power supply

In the format provided by the authors and unedited

Supplementary information: Cost and potential of metal–organic frameworks for hydrogen back-up power supply

Peng Peng,[1] Aikaterini Anastasopoulou,[1,2] Kriston Brooks,[3] Hiroyasu Furukawa,[4,5] Mark E. Bowden,[6] Jeffrey R. Long,[4,5,7] Tom Autrey,[6] Hanna Breunig[1*]

1. Energy Analysis and Environmental Impacts Division, Lawrence Berkeley National Laboratory, Berkeley, CA, USA

2. Department of Chemical and Biomolecular Engineering, University of Delaware, Newark, DE, USA

3. Energy and Environment Directorate, Pacific Northwest National Laboratory, Richland, WA, USA

4. Materials Sciences Division, Lawrence Berkeley National Laboratory, Berkeley, CA, USA

5. Department of Chemistry, University of California, Berkeley, CA, USA

6. Physical and Computational Sciences Directorate, Pacific Northwest National Laboratory, Richland, WA, USA

7. Department of Chemical and Biomolecular Engineering, University of California, Berkeley, CA, USA

*Correspondence: hannabreunig@lbl.gov

Contents

List of Supplementary Figures

List of Supplementary Tables

Nomenclature

Symbol	Definition	Unit
ρ_{sk}	Skeletal density	kg/m^3
$\rho_{crystal}$	Crystal density	kg/m^3
ρ_p	Pellet density	kg/m^3
ρ_{bulk}	Bulk density	kg/m^3
$\hat{\forall}_{pore}$	Pore volume per unit mass	m^3/kg
ε_b	Pellet porosity	
ε_p	Pellet porosity	
V_{bed}	Volume of the packed bed in the storage tank	m^3
$m_{H2\ per\ tank}$	Mass of H_2 stored per tank	kg
$m_{j-H2-solid}$	Mass of adsorped H_2 stored per tank	kg
$m_{j-H2-gas-tank}$	Mass of gas-phase H_2 stored per tank	kg
$m_{j-H2-gas}$	Mass of gas-phase H_2 fed by electrolyzer or fed to fuel cell	
m_{ads}	Mass of adsorbent per tank	kg
m_{vessel}	Mass of storage tank	kg
m_{excess}	Gravimetric excess H_2 uptake	g/kg or kg/kg
$\eta_{storage}$	% of bed filled	%
ρ_{H2}	Density of hydrogen	kg/m^3
m_{total}	Gravimetric total H_2 uptake	g/kg or kg/kg
$\hat{E}_{H2}$	Equivalent usage energy density of hydrogen	kWh/kg
E_{spec}	System-level specific energy	kWh/kg
E_{dens}	System-level energy density	kWh/L
n_{tank}	Number of storage tanks	
Capacity	Target H_2 capacity	kg
$m_{cap\ storage}$	Actual H_2 capacity	kg
$\Delta\hat{H}_{ads}$	Specific isosteric heat of desorption	kJ/kg

$\widehat{H}_{H_2}$	Specific enthalpy of H_2	kJ/kg
m_{MOF}	Mass of MOFs	kg
$\widehat{U}_{MOF}$	Specific internal energy of MOFs	kJ/kg
m_{wall}	Mass of the tank wall	kg
$\widehat{U}_{wall}$	Specific internal energy of the tank wall	kJ/kg
Cp_{solid}	Heat capacity of solid	kJ/kg·K
$Q_{\frac{cool}{heat}}$	Cooling or heating energy	kJ
Q_{loss}	Heat loss	kJ
W_S	Mechanical work by the compressor	kJ
R_0	Gas constant	kJ/mol·K
γ	Ratio of heat capacities	
MW_{H2}	Molecular weight of H_2	kg/mol
$\eta_{compressor}$	Compressor efficiency	%
$P_{compressor}$	Compressor power	kW
K_1, K_2, K_2	Cost parameters	
a, b	Refrigeration parameters	
$T_{Storage}$	Storage temperature	K
C_p^0	Capital cost	$
C_E^0	Energy cost	$
Cp_{MOF}	Heat capacity of MOFs	kJ/kg·K
$\Delta\widehat{H}_{ads}$	Heat of desorption	kJ/mol
Q_{heater}	Heater energy	kJ
P_{heater}	Heater power	kW
i	Real discount rate	
n	Number of operating years	
Tax	Tax rate	
D_{pv}	Present value of depreciation	
$P_{deliver}$	Delivered power	MW

CEPCI	Chemical Engineering Plant Cost Index	
CRF	Capital Recovery Factor	
DOD	Depth of discharge	%
n_{max}, α, β, P_0, V_a	Fitting parameters for the Dubinin-Astakhov model	
$A_1B_1C_1E_1$, $A_2B_2C_2E_2$	Fitting parameters for the dual-site Langmuir model	
$m_{released}$	Mass of H_2 released	kg
u_{des}	Velocity of releasing the hydrogen	m/s
S	Flow section	m^2
k	Rate of temperature increase	K/s

Note 1 System-level performance calculations

In general, an energy balance approach is used to calculate the energy and power requirements in each stage of operation. The analyses in this study are based on both experimental isotherms and adsorption performances from molecular simulation.

This note includes the detailed methods used to calculate the system-level performances of the MOF-based hydrogen back-up power system.

To convert the material properties of MOFs into bulk properties used in industrial applications, we first determine their skeletal density (ρ_{sk}) via Equation (1):

$$\rho_{sk} = \frac{1}{\frac{1}{\rho_{crystal}} - \hat{V}_{pore}} \quad (1)$$

where $\rho_{crystal}$ in kg/m^3 is the crystal density of the MOF, which is the commonly-reported value in literature. $\hat{V}_{pore}$ denotes the pore volume per unit mass in m^3/kg.

The pellet density (ρ_p in kg/m^3) and bulk density (ρ_{bulk} in kg/m^3) are determined based on the skeletal density, pellet porosity (ε_p), and bed porosity (ε_b) using Equations (2) and (3).

$$\rho_{bulk} = (1 - \varepsilon_b) \cdot \rho_p = \rho_p = (1 - \varepsilon_p) \cdot \rho_{sk} \quad (2)$$

The hydrogen gas capacity $m_{H2\ per\ tank}$ (kg) for each vessel is calculated from $m_{H2solid}$ and m_{H2gas}, which are the adsorbed (solid-phase) and gas-phase hydrogen in kg.

$$m_{H2\ per\ tank} = m_{H2solid} + m_{H2gas} \quad (3)$$

Here, $m_{H2solid}$ and m_{H2gas} are determined by Equations (4) and (5):

$$m_{H2solid} = \eta_{storage} \cdot m_{ads} \cdot m_{excess} / (\frac{1000g}{kg}) \quad (4)$$

$$m_{H2gas} = \eta_{storage} \cdot (V_{tank\_in} - \frac{m_{ads}}{\rho_{sk}}) \cdot \rho_{H2}(T,P)]/(\frac{1000g}{kg}) \quad (5)$$

where m_{ads} (kg) is the mass of MOFs stored in the tank, which is determined by Equation (6).

$$m_{ads} = V_{tank\_in} \cdot \eta_{pack} \cdot \rho_{bulk} \quad (6)$$

In Equations (4) to (6), V_{tank_in} is the internal volume (m^3) of the storage tank. The efficiency values $\eta_{storage}$ and η_{pack} are the storage efficiency and packing efficiency, respectively. $\eta_{storage}$ accounts for how much hydrogen is actually adsorbed respective to its theoretical limit. η_{pack} represents how much within the internal volume of the storage tank is used to pack the MOFs. In this analysis, both efficiencies are assumed to be 0.9 for both the solid (adsorbed) and gas phase hydrogen to account for the disk-shape heat exchangers for cooling and heating, and other minor devices that may occupy the tanks internal volume (i.e., valves and other supporting structures for the heat exchangers)[1-3].

m_{excess} is the excess hydrogen uptake of the MOFs in mg/g, which is defined as the difference in the total amount hydrogen in a defined system minus the amount of hydrogen in the same system and under the same conditions, but without adsorption[4]. In this analysis, m_{excess} is used to calculate the hydrogen adsorbed by the solid MOF pellets ($m_{H2solid}$ in Equation (4)), not counting those stored within the pores and empty volumes within the storage tank, which are defined as the gas-phase stored hydrogen (m_{H2gas}). m_{excess} is extrapolated from experimental isotherms, or modeled via molecular simulation depending on the type of MOFs discuss later in this note.

As mentioned in the main manuscript, we first compare multiple promising MOFs identified based on previous material-level screening.[5-8] The list of MOFs analyzed in this study is included in Supplementary Table 1. For Ni_2(m-dobdc) and V-btdd MOFs, we use experimentally generated pore volume, excess uptakes, and fitted isosteric heats of adsorption, as the input for the system and cost analyses. Note that the experimental excess uptakes here refer to the extrapolated values using the dual-site Langmuir model. Examples of extrapolation are shown later in Supplementary Fig. 7. The relationship between the absolute and excess uptakes described in this paper is shown in Equation (7), where V_{pore} (cm^3/g) is the pore volume of the MOF.[9,10]

$$m_{excess} = m_{total(abs\ in\ some\ paper)} - V_{pore} \cdot \rho_{H2}(T,P) \quad (7)$$

For the rest of the MOFs, we use the Monte-Carlo-based RASPA software[11] to run the molecular simulation to determine the excess uptake rate and isosteric heat of adsorption for the promising MOFs listed in Supplementary Table 1. The procedure and corresponding force field parameters are obtained from relevant literature.[9,11] The structural data (CIF) for these MOFs are downloaded from the Cambridge structural database.[12]

We compared the experimental results of V-btdd MOF with the simulated value from RASPA to ensure that the simulation uptakes fit the experimental results. Supplementary Fig. 1 shows that within the simulated temperature and pressure range in Fig. 2 of the main article, the comparison between the simulated hydrogen uptake achieves reasonable agreement with experimental results. We recognize there is a difference between the modeled and experimentally measured hydrogen uptakes. Since the simulated value is generally greater under the modeled storage range, the simulated value is used to calculate the theoretical storage potentials for the promising MOFs. For the same reason, experimentally extrapolated values from V-btdd and Ni_2(m-dobdc) were used for the detailed cost analysis and comparison with incumbent technologies.

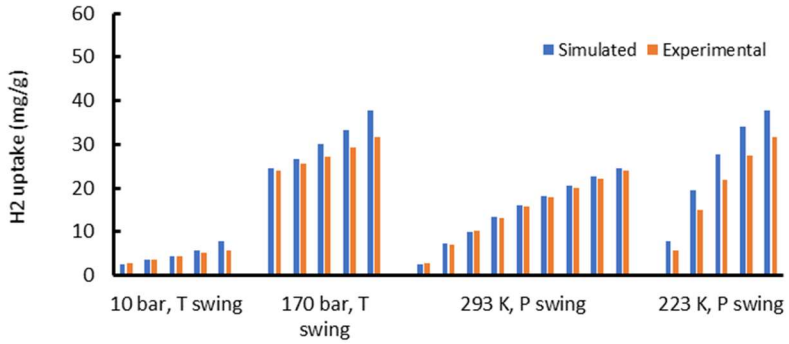

Supplementary Figure 1| Comparison of absolute H_2 uptake results between RASPA simulation and dual-site Langmuir fitting results. The experimental isotherms for V-btdd MOF are obtained under the conditions in Fig. 2 of the main text

Note that for the isosteric heat of adsorption, the value from RASPA simulation is lower than the experimentally fitted values (around 30% to 60% of the experimental value). The impacts on the cost analysis of these differences between the modelled and experimentally-derived isosteric heat of adsorption are neglected, as sensitivity analysis in later section (Supplementary Note 6) shows that the impact of the difference in isosteric heat of adsorption is less than 2% on the cost performance. Because of this, the cost impacts of the different isosteric heating values under different operation conditions are also neglected for V-btdd and Ni_2(*m*-dobdc).

Supplementary Table 1 | List of the Promising MOFs modeled in Fig. 2 of the main article

SNU-70	HKUST-1 (Cu-BTC)
NU-100	NOTT-112
MOF-5 (or IRMOF-1)	UiO-67
SUKYIH (Cu-based MOF)	Ni_2(m-dobdc)
CMOF-1a	V-btdd ($V_2Cl_{2.8}$(btdd))
$Zn_2(bdc)_2(dabco)$	

The material-level system performance is determined by normalizing the amount of hydrogen stored to the tank volume, vessel mass, and adsorbent mass. Particularly, the system-level specific energy (E_{spec} in kWh/kg) and energy density (E_{dens} in kWh/L) are determined in Equations (8) and (9):

$$E_{spec} = \frac{m_{H2\ per\ tank} \cdot \hat{E}_{H2}}{m_{ads} + m_{tank} + m_{H2\ per\ tank}} \quad (8)$$

$$E_{dens} = \frac{m_{H2\ per\ tank} \cdot \hat{E}_{H2}}{V_{tank\_out} \cdot \left(\frac{10^3 L}{m^3}\right)} \quad (9)$$

where m_{tank} and V_{tank_out} are the mass (kg) and outer volume (m^3) of the storage vessels, which are adjusted using the wall thickness and mass under each temperature and pressure condition determined from the Department of Energy Tankinator tool[13]. $\hat{E}_{H2}$(33.6 kWh/kg) is the standard energy density of hydrogen for specific energy and energy density conversion.[14]

Note 2 Cost analysis methodologies

Based on the system-level performance calculations, the number of tanks required to store the target capacity (≈ 90700 kg from Tables 1 and 2 of the main text) is determined in Equation (10)

$$n_{tank} = \frac{\text{Capacity}}{m_{H2\ per\ tank}} \quad (10)$$

which is rounded up to one integer. Due to this approximation, the actual stored capacity calculated via Equation (11) is slightly higher than the target capacity and is different between the MOF adsorbents.

$$m_{cap\ storage} = n_{tank} \cdot m_{H2\ per\ tank} \quad (11)$$

The total purchase cost of the tank (including liners and walls) is determined as the product of n_{tank} with the unit cost of each tank determined by the Tankinator model[13] under each specified storage condition (including liners and walls). The internal disks and fluid channels for heating and cooling are not included due to limited data available for scaling factor, and existing analysis shows they occupy a small amount of the tank cost (<5%), and may change dynamically with operation conditions[3].

The power and energy required to size and compute the capital costs of various unit operations are based on the energy balances between the different operation states in Fig. 1d of the main text. The enthalpy at each state (j) is calculated via Equation (12)

$$H_j = n_{tank} \cdot \{m_{j-H2-solid} \cdot [\Delta\hat{H}_{ads}(T_{j-tank}, P_{j-tank}) + \hat{H}_{H_2}(T_{j-tank}, P_{j-t}\quad)] + m_{j-H2-gas-ta}\quad \cdot \hat{H}_{H_2}(T_{j-tan}\ , P_{j-t}\quad) + +m_{j-H2-gas} \cdot \hat{H}_{H_2}(T_{j-gas}, P_{j-gas}) + m_{MOF}\hat{U}_{MOF}(T_{j-tank}, P_{j-tan}\ ) + m_{wall}\hat{U}_{wall}(T_{j-t}\quad, P_{j-tank})\} \quad (12)$$

where $\hat{H}_x$ designates the specific enthalpy of species x in kJ/kg, $\hat{U}_x$ is the specific internal energy in kJ/kg, which is the same as the specific enthalpy for solids such as the adsorbents and wall of the vessel. Again, $\Delta\hat{H}_{ads}$ (kJ/kg) is the heat of adsorption determined from the simulation and experimental results. Note that the specific heat of adsorption and desorption from the simulation had the unit of kJ/mol, and is converted into kJ/kg using the molecular weight of hydrogen (2.02×10^{-3} kg/mol). $m_{j-H2-solid}$ is the mass of solid-phase hydrogen adsorbed by the MOFs under state (j). $m_{j-H2-gas-tank}$ is the mass of gas-phase hydrogen stored in the tank under state (j). $m_{j-H2-gas}$ is the mass of gas-phase hydrogen outside of the tank (either fed from the electrolyzer or to the fuel cell) under state (j). T_{j-tank} P_{j-tan} are the temperature and pressure of all the solids, and gas-phase hydrogen, and solid-phase hydrogen in the tank after equilibrium is reached. T_{j-gas} and P_{j-gas} are the temperature and pressure of the gas-phase hydrogen outside of the storage tank, which can be either fed from electrolyzer, or to the fuel cell.

The thermodynamic properties for hydrogen gas under different operation conditions are determined from the National Institute of Standards and Technology (NIST) database using the Coolprop python package.[15] The sensible heat for cooling/heating the solids between the different states (j and i) is determined using a constant solid heat capacity during the adsorption and desorption. Since the temperature span in the main analysis did not reach the cryogenic region, such an approximation is a reasonable approach and has been used by several recent performance analyses of gas adsorption processes.[16,17]

$$\Delta\widehat{U}_{\mathrm{j,solid}} - \Delta\widehat{U}_{\mathrm{i,solid}} = \int_{T_i}^{T_j} \mathrm{Cp}_{\mathrm{solid}}\,\mathrm{dt} \quad (13)$$

The energy required to initial charge, charge, or discharge is estimated using the following energy balance Equation (14), assuming the kinetic energy and potential energy terms are neglected:

$$H_f - H_i = W_S + Q_{\underline{\text{cool}}\atop\text{heat}} + Q_{\mathrm{loss}} \quad (14)$$

where H_f and H_i are the final and initial enthalpies calculated using Equation (12) under different stages described in Fig. 1d of the main text. The temperature and pressure conditions for the final and initial states for different charging and discharging cycles are shown in listed in Supplementary Table 2, with illustrations shown in Supplementary Fig. 2.

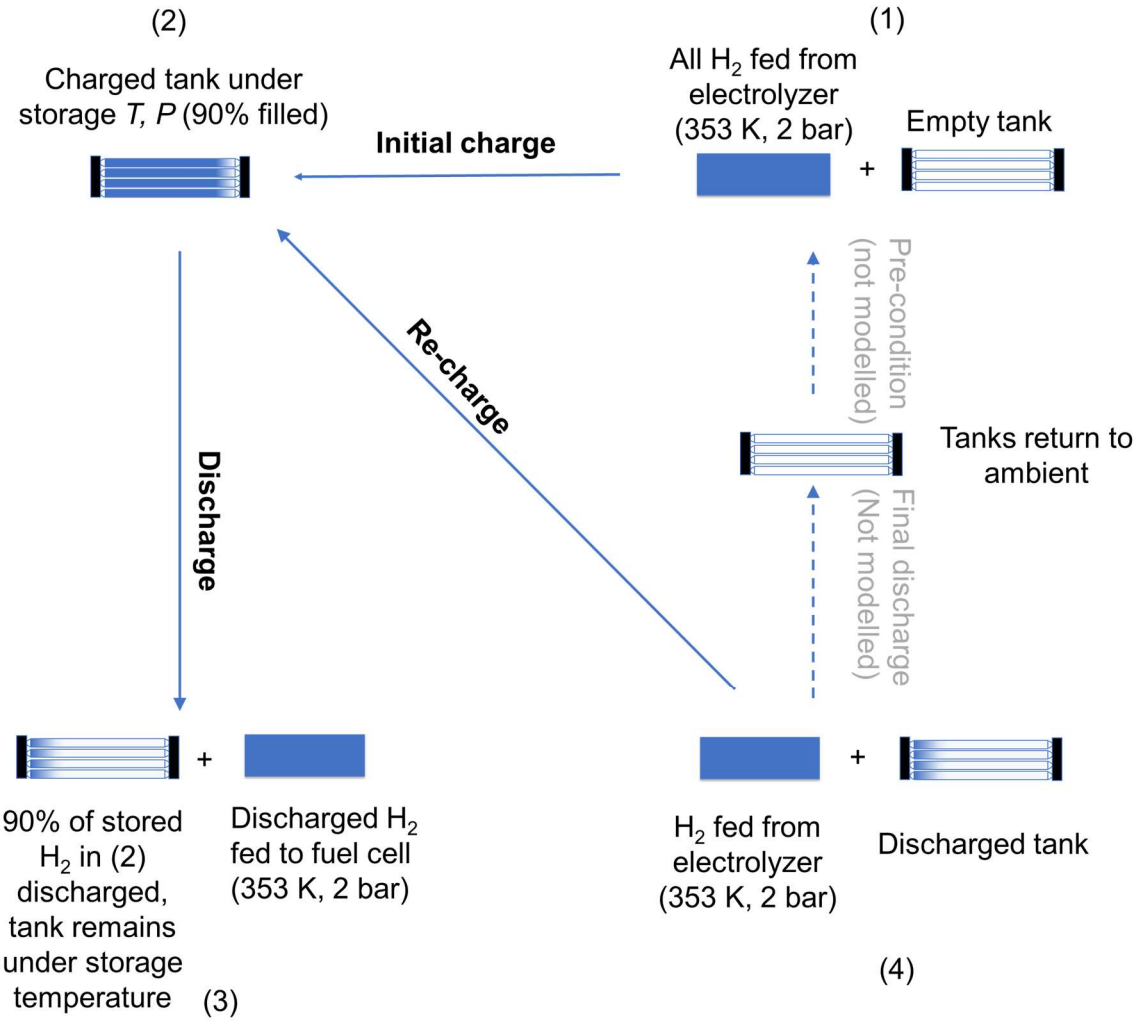

Supplementary Figure 2 | Detailed illustrations of the charge and re-charge states in Fig. 1d of the main text

Supplementary Table 2 | Detailed parameters for each charge and re-charge state in Fig. 1d of the main text

State	(1)	(2)	(3)	(4)
$m_{j-H2-solid}$	0	$m_{H2solid}$	$(1-DOD)\cdot m_{H2solid}$	$(1-DOD)\cdot m_{H2solid}$
Comment	Empty tank	Adsorbed solid-phase H_2 in the tank as calculated in Equation (4)	Remaining H_2 in left in the tank	Remaining H_2 left in the tank
$m_{j-H2-gas-tank}$	0	m_{H2gas}	$(1-DOD)\cdot m_{H2gas}$	$(1-DOD)\cdot m_{H2gas}$
Comment	Empty tank	gas-phase H_2 in the tank as calculated in Equation (5)	Remaining H_2 left in the tank	Remaining H_2 left in the tank
$m_{j-H2-gas}$	$m_{cap\ storage}$	0	$DOD\cdot(m_{H2gas}+m_{H2solid})$	$DOD\cdot(m_{H2gas}+m_{H2solid})$
Comment	All gas is fed from electrolyzer	All gas stored in the tank	Discharged gas fed to fuel cell	Recharged gas fed from electrolyzer
$\boldsymbol{T_{j-tank}}$	N/A (no need to specify)	293 K-223 K	293 K-223 K	293 K-223 K
Comment	Empty tank	Storage temperature	Storage temperature	Storage temperature
$\boldsymbol{P_{j-tank}}$	N/A	10 bar-170 bar	$(1-DOD)\cdot P_{2-tank}$	$(1-DOD)\cdot P_{2-tank}$
Comment	Empty tank	Storage pressure	Remaining pressure under ideal gas assumption	Remaining pressure under ideal gas assumption
$\boldsymbol{T_{j-gas}}$	353 K	N/A	353 K	353 K
Comment	Feed temperature from electrolyzer	All gas in the tank	Discharged H_2 fed to fuel cell	Feed temperature from electrolyzer
$\boldsymbol{P_{j-gas}}$	2 bar	N/A	2 bar	2 bar
Comment	Feed pressure from electrolyzer	All gas in the tank	Discharged H_2 fed to fuel cell (or from electrolyzer)	Feed pressure from electrolyzer

In Equation (14), W_S is the mechanical work required by the compressor to compress the hydrogen to the desired storage pressure, and $Q_{cool/heat}$ is the cooling and heating energy requirements. During the charge and discharge the dynamic heat loss is not modelled. Therefore Q_{loss} is zero during the charge and discharge. For the compressor, the work required in kJ/kg is determined by Equation (15); another similar formula for compressor sizing led to similar results.[18,19] Since the hydrogen generation and conversion

systems are assumed to be on-site and co-located with the storage system, the related energy required to transport the hydrogen in the pipeline is assumed to be included within the 70% efficiency of the compression unit.

The amount of hydrogen leftover in the tank in both the solid and gas phases is 10% of the amount when fully loaded at the storage temperature and pressure. Note that under low-pressure storage conditions (10 bar), 90% of DOD is less than the fuel cell pressure. In this case, the fuel cell pressure is used as the remaining tank pressure after the discharge ($P_{3-\mathrm{ta}}$). The minor inconsistency between the actual storage capacity required versus what is calculated using Equation (10) is neglected for the 10 bar storage conditions.

$$\mathrm{W_s} = \mathrm{n_{tank}} \cdot (\mathrm{m_{H2\ per\ tank}}) \cdot \frac{\mathrm{R_0}}{\mathrm{MW_{H2}}} \frac{\gamma}{\gamma-1} \cdot ((\frac{\mathrm{P_{out}}}{\mathrm{P_{in}}})^{\left(\frac{\gamma-1}{\gamma}\right)} - 1) \quad (15)$$

Based on the compression power requirements the assumed compressor efficiency, the compressor is sized from the required power (kW) based on Equations (16) and (17):

$$\mathrm{P_{compressor}} = \frac{\mathrm{m_{cap\ storage}} \cdot \mathrm{W_s}}{\eta_{\mathrm{compressor}} \cdot \mathrm{t_{charge}} \cdot \frac{3600\mathrm{s}}{1\ \mathrm{h}}} \quad (16)$$

$$\log_{10} \mathrm{C^0_{p\_compressor}} = \mathrm{K_1} + \mathrm{K_2} \log_{10}(P_{\mathrm{compressor}}) + \mathrm{K_3}[\log_{10} P_{\mathrm{compressor}}]^2 \quad (17)$$

where η is the efficiency of the compressor. $K_1 = 2.2897$, $K_2 = 1.3604$, and $K_3 = -0.1027$ are the correlation parameters for the purchase equipment cost.[20] t_{charge} (h)is the target charging time.

To save computational cost, the internal mass and heat transfer effects during the adsorption and desorption and their impacts on the actual charging and discharging ($t_{discharge}$) times between different MOFs are not included in this study. A representative example of modeling the mass transfer effects could be found in our earlier study.[21]

The energy requirement of the heater is determined using a similar fashion. The efficiency of the heater is assumed to be 0.7, accounting for the heat loss during this process. For the heating unit, the cost parameters K_1, K_2, and K_3 in Equation (17) are 6.9617, –1.48, and 0.3161, respectively.[20] The energy required from the heater is calculated by Equation (18) from the energy balance and the power, and the power used to size the heater is calculated from its efficiency and target charging time in Equation (19). Based on our previous analysis,[21] the actual charging rate might differ from the input charging time due to mass and heat transfer effects within the storage tanks. We recognize that the charging time could potentially be longer than what is set as the target, and are slightly different based on the type of MOFs and adsorption mechanisms. The details of these effects are not included as it is not the focus of this study.

$$Q_{\mathrm{heater}} = H_{\mathrm{f}} - H_{\mathrm{i}} - W_{\mathrm{s}} \quad (18)$$

$$\mathrm{P_{heater}} = \frac{\mathrm{Q_{heater}}}{\mathrm{t_{discharge}} \cdot \frac{3600\mathrm{s}}{1\ \mathrm{h}} \cdot \eta_{\mathrm{heater}}} \quad (19)$$

For refrigeration, the capital cost and energy cost are determined from the storage temperature ($T_{Storage}$ in K) from Equations (20)–(22), which are fitted using the capital cost (C^0_p in $) and refrigeration energy cost (C^0_E in $/GJ) data extracted from Luyben 2017.[22]

$$\mathrm{C^0_p} = \mathrm{a T_{Storage}}^{\mathrm{b}} \quad (20)$$

For $C^0_{p\_refrigeration\_1MW}$: $a = 2E11,\ b = -2.077$ (21)

For $C^0_{E\_refrigeration\_1MW}$: $a = 4E7,\ b = -2.669$ (22)

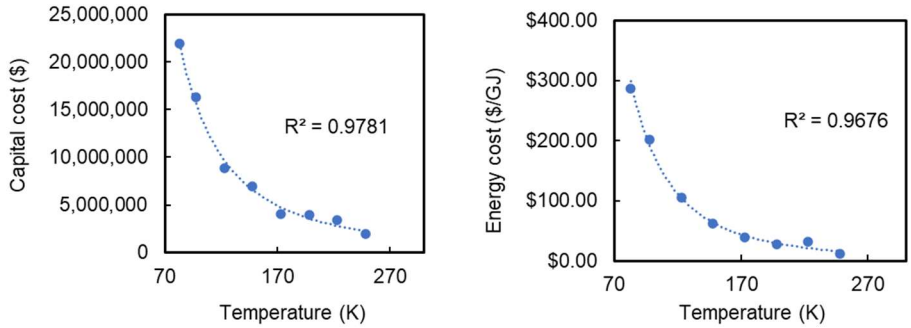

Supplementary Figure 3 | Correlations of capital and energy cost for 1 MW refrigerators with respect to the cooling temperature. Data extracted from Luyben 2017.[22]

Note that Equations (17) to (18) are derived for 1 MW refrigeration systems. To convert the refrigeration capital cost for this study, Equation (23) is used, using the 0.6 scale factor recommended by Luyben 2017,[22] in the case where $P_{Initial\ charge} > P_{Charge}$. Also, note that the electricity cost used in Luyben 2017 is \$16.8/GJ, which is equivalent to \$0.06/kWh.

$$C^0_{p\_refrigeration} = C^0_{p\_refrigeration\_1MW} \cdot \left(\frac{P_{initial\ charge}}{1000\frac{kW}{MW}}\right)^{0.6} \quad (23)$$

The energy cost for the refrigeration system in this study is determined by the energy ($C^0_{E\_refrigeration}$ in \$/GJ) consumed during both the initial charge and charging phases (Equation (24)). In this study, we assume that the operation costs for compressor, refrigeration, and heater comprise the energy cost. As a one-time inventorying material, the cost of purchasing the refrigerant could be neglected to compare with the capital cost and energy cost.[22]

$$C^0_{E\_refrigeration} = C^0_{E\_refrigeration\_1MW} \cdot (E_{initial\ charge} + E_{charge}) \quad (24)$$

Finally, the levelized cost of energy is determined based on the annual storage capacity using Equations (25) and (26) from the Capital Recovery Factor (CRF). The number of operating years (n), and the real discount rate (j), tax rate (tax), and the present value of depreciation (D_{pv}) were determined from the latest NREL's Energy Analysis documentations.[23]

$$CRF = \frac{j(1+j)^n}{(1+j)^n - 1} \quad (25)$$

$$LCOS = \left(\frac{(\sum C^0_p)\cdot CRF\cdot(1-Tax\cdot D_{pv})}{\text{Annual } H_2 \text{ capacity}\cdot(1-Tax)} + \frac{\sum \text{Annual O\&M Costs}}{\text{Annual } H_2 \text{ capacity}}\right)/(\widehat{E}_{H2}) \quad (26)$$

The annual hydrogen capacity is estimated using Equation 27 from the actual hydrogen stored on-site ($m_{cap\ storage}$), number of annual operation cycles (n_{cycles}), and the depth of discharge (DOD) for each cycle l. In this study, we set our target storage duration as 96 hours to meet the standard for emergency and standby power systems requirement for critical infrastructure by the National Fire Protection Association.[24] 90% for regular 96-hour discharge capacity base case study. As discussed in the main text, we assume 240

hours of annual storage duration as the base case, which can be distributed flexibly among different cycles in Equation (27), as long as all the prior calculations made are based on 96-hour storage capacity.

$$\text{Annual } H_2 \text{ capacity} = m_{\text{cap storage}} + \sum_{l=1}^{l=n_{cycles}-1} m_{\text{cap storage}} \cdot \text{DOD}_l \quad (27)$$

When comparing the cost performance between this study and the other contemporary incumbent energy storage technologies, the system costs normalized to the per kWe discharge, and kWh of energy stored are used. As shown in Equations (28), only the capital investments are compared when calculating the system cost to avoid inconsistency drawn from the assumptions from operation costs, depth of discharge, etc. For comparing incumbent technologies, system costs listed in the Pacific Northwest National Laboratory (PNNL)'s 2020 Grid Energy Storage Technology Cost and Performance Assessment are used.[25] When making the comparison, the indirect and direct (i.e., system integration) is assumed to be 0.4.[25]

$$\text{System cost (\$/kW)} = \frac{\sum C_p^0}{P_{\text{deliver}}(10 \text{ MW in this study})} \quad (28)$$

Note 3 Additional assumptions and cost factors

The key assumptions for the above-mentioned cost analysis are included in Tables 1 and 2 in the main text. Other additional assumptions and the cost factors used are summarized in the following Supplementary Table 3. Note that maintenance is assumed to be 3% of the total capital cost,[26,27] and MOF cost is included when calculating the maintenance for MOF storage in order to make a fair comparison with the compressed gas storage.

Note that there is a nationwide variation from 0.02 to 0.1 $/kWh for the wholesale electricity cost based on the geographical and seasonal differences. The 0.067 $/kWh value we use in this study is relatively conservative as most wholesale prices are between 0.02–0.07 $/kWh.[28]

The labor cost for this back-up power system requires unique consideration. Equations (29) and (30) are used as the basis to calculate the labor required for the system, using the equivalent equipment module approach.[20]

$$N_{OL} = [6.29 + (0.23 \cdot N_{Np})]^{0.5} \quad (29)$$

$$C_{p\_latbor}^0 = N_{OL} \cdot \text{working hours per year} \cdot 36 \text{ \$/hr} \cdot 2 \quad (30)$$

Here, we assume that the back-up system is well-designed so that for year-round monitoring and usage, each type of unit operation can be considered as one piece of equipment using Equation (29) accounting for contingency, worker benefits, etc. Thus N_{Np}= 4 (for compressor, storage tank, refrigerator/heater, electrolyzer/fuel cell) was used for year-round monitoring/maintenance (350 working days per year, and 24 hours per day).

We also made another calculation assuming 100 pieces of equipment (estimation of the number of compressors, refrigerators, and heaters) during the back-up cycles. In this case, N_{Np}=100. The hours of operation are 240 hours per year for the base case.

The labor cost calculated for the first case (year-around operation for 4 pieces of equipment) is $1,600,000 per year and $94,000 per year for the second case (240-hour operation for 100 pieces). We selected the average value for the labor cost for this back-up power system. 1-4% of uncertainty in LCOS in the base case depending on the temperature and pressure conditions.

Supplementary Table 3 | Key cost factors for the TEA analysis in this study

Cost factor	Value	Reference
Life time (years)	30	This study
Real discount rate (%)	7	NREL, 2020[23]
Tax rate (%)	38.9	NREL, 2020[23]
Present value of depreciation	0.83	NREL, 2020[23]
MOF cost ($/kg)	25	El-Sayed and Yuan, 2020[29]; DeSantis et al., 2017[30]
Energy cost ($/kWh) for charging the storage system	0.067 $/kWh	EIA, 2021[28]
Operational labor wage ($/h)	36 $/h	US Bureau of Labor Statistics[31]
Maintenance (%)	3 %	
CEPCI 2001	397	Turton et al., 2018[20]
CEPCI 2007	525	Turton et al., 2018[20]
CEPCI 2019	607	Turton et al., 2018[20]
CEPCI 2020	614	Jenkins, 2020[32]
Inflation	1.2%	US Bureau of Labor Statistics
Direct and indirect costs for fixed capital investment (e.g., Installation, back-up, contingency, piping, legal and contractor fees)	0.52 of capital	Spurgeon et al., 2018[33]; Shaner et al., 2016[34]; James et al. 2013[35]; Colella et al. 2014[36]

For heat transfer with the ambient of each storage tank, the conductive heat transfer between the bulk storage tank system and the ambient, and its relation with the insulation thickness is studied. The effects of internal conductive heat transfer, or convective heat transfer during charging and discharging are not modelled. Heat loss rate per area (P_{loss} in W) between the storage tanks and ambient is estimated by Equation (31) via conduction through the cylindrical tank wall[18]:

$$\frac{dQ_{\text{loss}}}{dt} = P_{\text{loss}} = (T_{\text{storage}} - T_{\text{amb}})/[(\frac{\ln\left(\frac{r_{\text{tank}_o}}{r_{\text{tank}_i}}\right)}{2\pi k_{\text{tank}} L_{\text{tank}}}) + (\frac{\ln\left(\frac{r_{\text{ins\_o}}}{r_{\text{ins\_i}}}\right)}{2\pi k_{\text{ins}} L_{\text{tank}}})] \quad (31)$$

where $r_{\text{tank\_o}}$ and $r_{\text{tank\_i}}$ are the outer and inner radiuses of the insulation layer, which are 0.31 m and 0.3 m, respectively, as determined from the Tankinator tool.[13] T_{storage} is the storage temperature (K) in the standby mode (refer to state 2 in Fig. 1d of the main text), and T_{amb} is the ambient temperature , which is set as 298 K. k_{tank} and k_{ins} are the thermal conductivities of the storage tank and insulation material, which are 239 W/m·K for type I aluminum tank and 0.004 W/m·K for common multi-layer vacuum insulations.[37-39]

The cost of insulation is calculated by Equation (32).

$$C^0_{p\_ins} = \frac{54\ \$}{kg} \cdot \pi \cdot ({r_{ins_o}}^2 - {r_{ins_i}}^2) \cdot L_{tank} \cdot \rho_{ins} \cdot 1.9 \quad (32)$$

where ρ_{ins} is the density of the of multi-layer vacuum insulation (60 kg/m^3), 54 \$/kg is its unit cost (2010 value), and 1.9 is the process and installation factor.[40]

During the stand-by mode, Equation (11), $H_f - H_i$ and W_s are zero because the storage condition does not change and no mechanical work is done. Therefore, Equation (11) is reduced to $-Q_{loss} = Q_{cool}$.

During the standby mode, the heat loss rate $\dot{Q} = \frac{dQ_{loss}}{dt}$ is constant, therefore

$$Q_{loss} = \dot{Q} \cdot t_{storage} \quad (33)$$

where $t_{storage}$ is the storage time (h), which can be determined from Equation (34).

$$t_{storage} = \left[360 \cdot 24 - n_{cycles} \cdot \left(t_{discharge} + t_{charge}\right)\right]/n_{cycles} \quad (34)$$

Where n_{cycles} is the number of operation cycles per year, and $t_{discharge}$ is the target discharge time (h), and t_{charge} is the target charging time (h).

The cost required to maintain the storage temperature ($C^0_{E\_loss}$) during each cycle is calculated by Equation (35).

$$C^0_{E\_loss} = Q_{loss} \cdot n_{tank} \cdot P_{electricity} \quad (35)$$

where $P_{electricity}$ is the electricity cost (\$/kWh), which is 0.067 \$/kWh for the base case.

As shown in Supplementary Fig. 4, insulation cost and energy cost to maintain the storage temperature during standby are highly related to the amount of insulation materials used for the storage system, which in this analysis is represented by the thickness of the insulation material. Supplementary Fig. 4a shows the tradeoff between $C^0_{p\_ins}$ and $C^0_{E\_loss}$ when amount of insulation material is used under two representative storage conditions (293 K and 170 bar, 223 K and 170 bar, and 77 K and 170 bar). Under both conditions, increasing the amount of insulation materials requires higher capital cost, but requires less energy/operation cost to maintain the storage temperature to compensate heat transfer with the ambient. Under higher temperature conditions, more storage tanks are required since gas phase hydrogen density and uptake by the MOFs are both reduced. Therefore, the capital cost to purchase the insulation materials are higher. On the other hand, the driving force of heat transfer, which is the gradient between the storage temperature and the ambient, decreases in higher storage temperatures. Thus, the cost of maintenance is lower when the storage temperature is closer to the ambient.

Based on the tradeoffs discussed above, Supplementary Fig. 4b show how the optimal LCOS can be reached by controlling the thickness of insulation materials. The general trend is that when the storage temperature is higher, the theoretical optimal thickness is higher to offer minimum cost. Under all three cases, the optimal cost associated with insulation and maintaining the storage temperature accounts is non-monotonic with temperature and the optimum conditions change dynamically with the storage conditions. Under optimal conditions, costs associated with insulation and maintaining temperature account for only small amount within the total LCOS (Supplementary Fig. 4b), and the thickness of insulations has negligible effects on the system-level energy density (Supplementary Fig. 4c), Thus, to reduce computational cost in calculations, these effect are not modelled for the rest of the analysis.

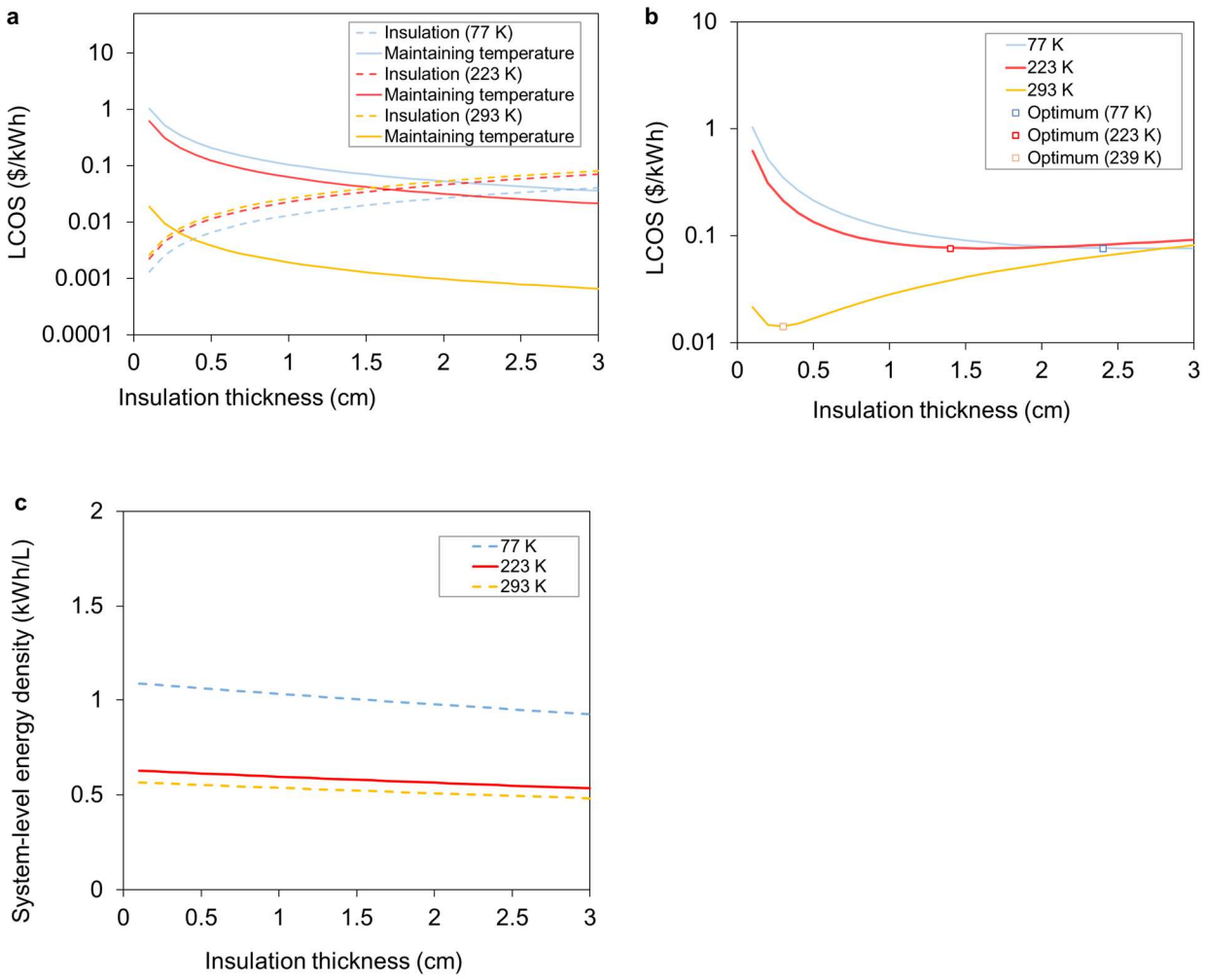

Supplementary Figure 4 | Capital cost of insulation and operational cost of maintaining storage temperatures for Ni_2(m-dobdc) with different thickness of insulation materials under 223 K and 77 K (both 170 bar) storage conditions. a, Breakdown and tradeoffs of LCOS. **b,** Total LCOS of insulation and maintaining temperature during storage. **c,** System-level energy density.

Note 4 Cost breakdowns and tradeoffs

Supplementary Table 4 below shows a cost breakdown, as well as the key system-level performance parameters of the Ni_2(m-dobdc) under different storage temperatures and pressures. This table serves as a supplement to Fig. 3a of the main text and a reference for the scale of CAPEX and OPEX for different components. From the results, the CAPEX and OPEX for the heater are very small compared with the rest of the components.

In terms of the cost breakdown, liquid hydrogen storage under high-pressure conditions is not favored mainly due to the cost associated with the cryogenic refrigeration of on-site generated hydrogen (Fig. 3a of main text). For Comp-H_2 storage, the compressor is the costliest component for the Comp-H_2 storage to pressurize the hydrogen from around atmospheric pressure to 350 bar. According to the Tankinator

model, the cost of storage tanks increases significantly with pressure (~$9000/tank at 170 bar for Type I, and ~$20,000 at 350 bar for Type IV).[13]

Supplementary Table 4 | Cost breakdown of Ni_2(*m*-dobdc) under the representative storage temperatures and pressures

LCOS breakdowns ($/kWh)	Others	Compressor	Tank	Refrigeration	Heater	MOF Cost	O&M
High porosity MOFs							
223 K 170 bar	1.08	0.40	0.23	0.65	0.0049	0.78	0.83
293 K 170 bar	1.14	0.40	0.34	0.35	0.0041	1.09	0.87
223 K 10 bar	3.27	0.09	0.08	0.40	0.0063	5.71	2.25
293 K 10 bar	7.49	0.09	0.21	0.19	0.0046	13.91	4.96
Low porosity MOFs							
223 K 170 bar	1.63	0.40	0.14	0.69	0.0067	1.90	1.20
293 K 170 bar	2.09	0.40	0.24	0.38	0.0059	2.99	1.48
223 K 10 bar	4.44	0.09	0.03	0.44	0.0073	7.96	3.00
293 K 10 bar	15.47	0.09	0.11	0.23	0.0063	29.32	10.13
Reference methods							
Comp-H_2 (293 K, 350 bar)	0.70	0.59	0.34	0.42	0.0032	N/A	0.59
Comp-H_2 (293 K, 170 bar)	0.55	0.45	0.25	0.36	0.0032	N/A	0.48
Liq-H_2 (19 K, 1 bar)	23.53	0.00	0.00	45.24	0.0056	N/A	17.70

Note 5 Footprint

The design of hydrogen storage tanks can have different length to diameter ratio from 3 to 37[41,42], which has negligible effect to the energy density as the tanks have the same volume (~3 m^3 internal). The wall For this analysis, a representative value of 15 is selected. The size of the storage system can be estimated based on the number of tanks calculated from Equations (1) to (10). As shown in Supplementary Fig. 5a to Supplementary Fig. 5c, the tanks are modeled as hollow cylinders installed on cuboid racks. Note that minor gaps between storage tanks shown in Supplementary Fig. 5a to Supplementary Fig. 5c are not included in the energy density calculation in Supplementary Note 1 and in Fig. 2 of the main text for the broader analysis under different temperature and pressures.

The number of storage tanks installed in the *x*, *y*, and *z* directions can be adjusted to give a cubical storage system. For the dimensions used in this analysis, the ratio of number of tanks stored in the *x*, *y*, and *z* directions are approximately 15:15:1. Listed in Supplementary Table 5 are the tank design parameters from the system analysis for the promising MOF Ni_2(*m*-dobdc) compared with compressed hydrogen storage.

Supplementary Table 5 | Footprint comparison results between Ni_2(*m*-dobdc) and compressed hydrogen storage. Tank thicknesses for both length and radius under different conditions are determined from the Tankinator model[13].

Conditions	Ni_2(*m*-dobdc) 170 bar, 223 K, bed porosity 0.6	Ni_2(*m*-dobdc) 170 bar, 223 K, bed porosity 0.2	Compressed H2 170 bar 293 K	Compressed H2 350 bar 293 K
Number of tanks	1600	980	2100	1100
Tank type	Type I	Type I	Type I	Type IV
Height to width ratio	15	15	15	15
Tank inner diameter (m)	0.62	0.62	0.62	0.62
Tank outer diameter (m)	0.69	0.69	0.69	0.67
Tank inner length (m)	10	10	10	10
Tank outer length (m)	10.07	10.07	10.07	10.05

Shown in Supplementary Fig. 5d, the reduction of required number of tanks to store the target amount of hydrogen can be directly translated to the reduced of footprint. Both packing porosities (0.6, 0.2) under the base case condition (170 bar, 223 K) require less footprint compared with compressed hydrogen storage under the same pressure condition. As shown in Fig. 2 of the main text, the energy density of Ni_2(*m*-dobdc) is exceeds compressed H_2 tanks under 350 bar, requiring less than 80% of the volume to store the same amount of hydrogen (~90,700 kg for 10 MW deliverable power).

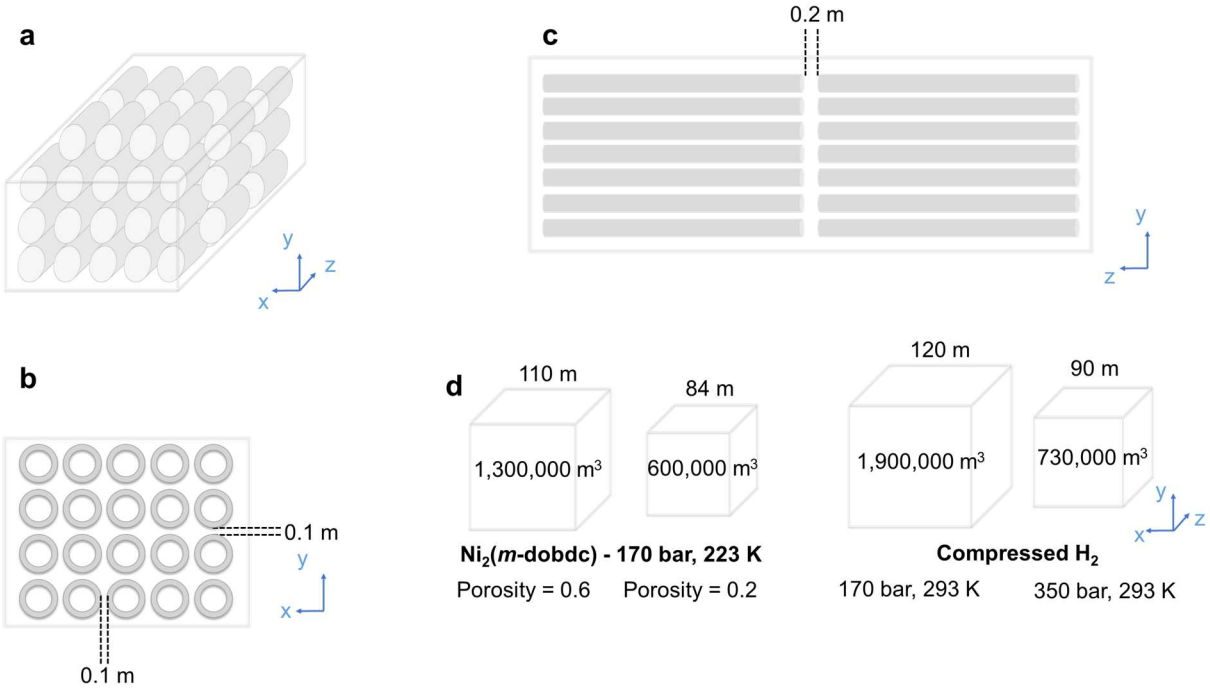

Supplementary Figure 5 | Results of footprint analysis. a, 3-D illustration of how MOF tanks are stored. **b,** front-view of the storage system. The dimensions are shown are for Type I storage tanks under 170 bar, 223 K, as determined from the Tankinator model. **c,** side view of the storage system. **d,** relative volume and dimensions of MOF H_2 storage vs. compressed H_2 storage under representative conditions. Shapes are for illustrative purpose only. Relative sizes should refer to the labelled numerical values and Supplementary Table 5.

Note 6 Sensitivity analysis

For the sensitivity analysis, the upper and lower bounds of various critical parameters are included in the Supplementary Table 6.

Supplementary Table 6 | Base case values, as well as upper and lower boundaries for sensitivity analysis.

Value	Base value	Economical case	Expensive case	Reference for base value
m_{excess} (g/kg)	13	21	5	Experimental isotherms
Cp_{MOF} (J/kg·K)	900	360	1440	Wieme et al., 2019 [43]
$\Delta\hat{H}_{ads}$ (kJ/mol)	–12	–5	–20	Kapelewski et al., 2014[44]
MOF cost ($/kg)	25	10	40	El-Sayed et al., 2020[29]; DeSantis et al., 2017[30]
Target charging time (h)	4	6.4	1.6	This study

Supplementary Fig. 6 shows the sensitivity of results to target charging time, as well as several critical material properties: MOF cost, excess uptake, the heat of adsorption, and heat capacity. For each variable, a 60% variation is used for both the upper and lower bound of the analysis compared to the base case value. From this Supplementary Fig. 6, target charging time, MOF cost, and excess uptakes are the most influential factors for the cost performance, therefore are chosen for further detailed studies.

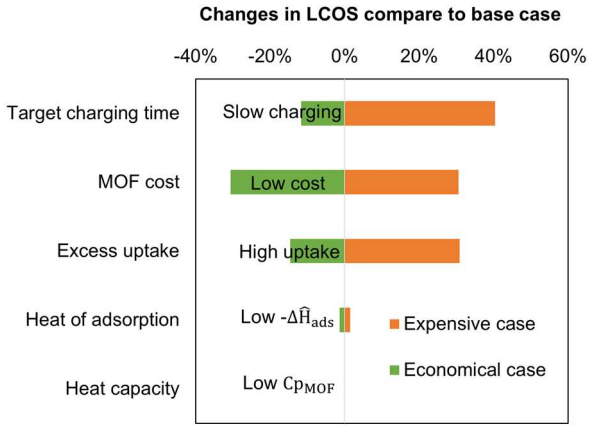

Supplementary Figure 6 | Sensitivity analysis of MOF H_2 storage system for back-up power applications.

Note 7 Modeling the discharging behaviors

We modeled the desorption process under both pressure swing and temperature-programmed desorption scenarios to make sure that the modeled system in this study could meet the discharge requirements by the end user, which is providing 10 MW of back-up power for 96 hours. For this study, we use a modified Dubinin-Astakhov (DA) model[45,46] to analyze the discharge behavior of MOFs for the back-up power application. The adsorption form of the DA model is represented by Equation (36):

$$m_{total} = MW_{H2} \cdot \left[n_{max} \exp\left(-\frac{RT}{\alpha+\beta T}\right)^2 \ln^2\left(\frac{P_0}{P}\right) - \rho_{H2} \cdot V_a\right] \quad (36)$$

where m_{total} (g/kg) is the total adsorbed hydrogen. MW_{H2} (kg/m^3) is the molecular weight of hydrogen, and R (J/mol·K) is the gas constant. T (K) and P (Pa) are the temperature and pressure of the storage system. n_{max}, α, β, P_0, V_a were the model parameters are determined based on fitting the model to experimental isotherms.

Among the different models used to describe adsorption isotherms, we select the modified DA model to save computational cost while retaining high accuracy. Specifically, when analyzing the discharging behavior of the system, we find the modified DA model could be reversed at a much lower computational cost compared with other isotherm models with similar accuracy. To validate the reliability of the modified DA model, we compare the fitting results of the modified DA model with results generated using the dual-site Langmuir model, which is known to provide high accuracy. The dual-site Langmuir model is described by Equation (37),[21] where the dual-site Langmuir parameters ($A_1, B_1, C_1, A_2, B_2, C_2$) are determined using the same experimental data sets as the modified DA model.

$$m_{total} = \frac{A_1 B_1 C_1 \exp\left(-\frac{E_1}{RT}\right) P}{1 + B_1 C_1 \exp\left(-\frac{E_1}{RT}\right) P} + \frac{A_2 B_2 C_2 \exp\left(-\frac{E_2}{RT}\right) P}{1 + B_2 C_2 \exp\left(-\frac{E_2}{RT}\right) P} \quad (37)$$

In terms of accuracy, Supplementary Fig. 7 shows the fitting results of both the modified DA model and the dual-site Langmuir model using experimental isotherms of V-btdd MOF under various temperatures. The root mean square error (RMSE) value of the modified DA model is similar to the dual-site Langmuir model. Therefore, the modified DA model provides enough accuracy to model the adsorption and desorption behavior of MOFs for the purpose of this study.

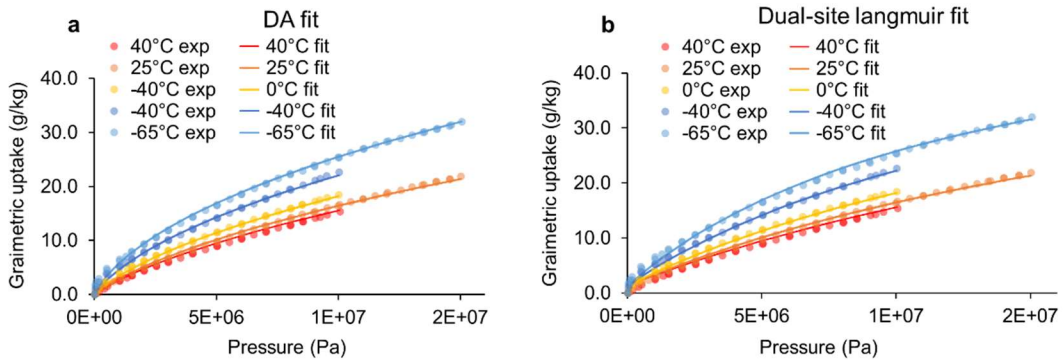

Supplementary Figure 7 | Comparison of fitting results for the total gravimetric uptake rates of V-btdd adsorption isotherms under various temperatures using a, modified DA model, and b, Dual-site Langmuir model.

Beyond the desorption kinetics of H_2 from MOFs, the hydrogen outflow velocity (u_{des} in m/s) could be calculated based on the pressure difference between the storage vessel (P_2) and fuel cell (P_3), as shown from a dynamic energy balance in Equation (38).[45,46] Equation (38) is integrated over the modeled discharge time to calculate the total amount of hydrogen released in Supplementary Fig. 8a. The hydrogen release rate ($\frac{dm_{released}}{dt}$ in kg/s) during the discharge is calculated from equation (38) using the velocity, hydrogen density, and flow section at the exit of the storage vessel S (m^2).

$$\frac{dm_{released}}{dt} = u_{des}(t, m_{total}) \cdot \rho_{H2} \cdot S \cdot MW_{H2} \quad (38)$$

$$u_{des} = \sqrt{\frac{2(P_2 - P_3)}{MW_{H2} \cdot \rho_{H2}}} \quad (39)$$

P_2, the instantaneous pressure in the storage vessels, is determined by reversing the modified DA model[45,46] shown in Equation (40), where n_{max}, α, β, P_0, V_a are obtained from the fitted experimental isotherms.

$$P_2(T, m_{total}) = P_3 / \exp\left[\frac{\sqrt{\ln\left(\frac{n_{max}}{\frac{m_e}{MW_{H2}} + \rho_{H2} \cdot V_a}\right)}}{\left(\frac{RT}{\alpha + \beta T}\right)}\right] \quad (40)$$

We modeled the temperature-programmed desorption by employing first-order heating with a constant heating rate ($k = \frac{dT}{dt}$ in K/s). Note that as the pressure decreased during the discharging process, the hydrogen release rate would reach its maximum value regardless of whether the vessel was heated. Therefore, a control block was added to the model so that the heating rate (k) automatically becomes zero

when $\frac{d m_{released}}{dt} = 0$, which could be shown in Supplementary Fig. 8c. As shown in this model, there are only limited effects to add temperature-swing desorption; therefore, it is not introduced in the TEA in this study. On the other hand, the ideal desorption should be a controlled release with a steady desorption rate based on the end-application requirement, as shown in Supplementary Fig. 8d. In this study, we assume that this could be achieved via well-designed feedback control (i.e., between the hydrogen flow controllers and flow section of the storage tank). The desorption model is not related to the cost analysis, as we assume the process control could be well designed to offer a steady release of hydrogen.

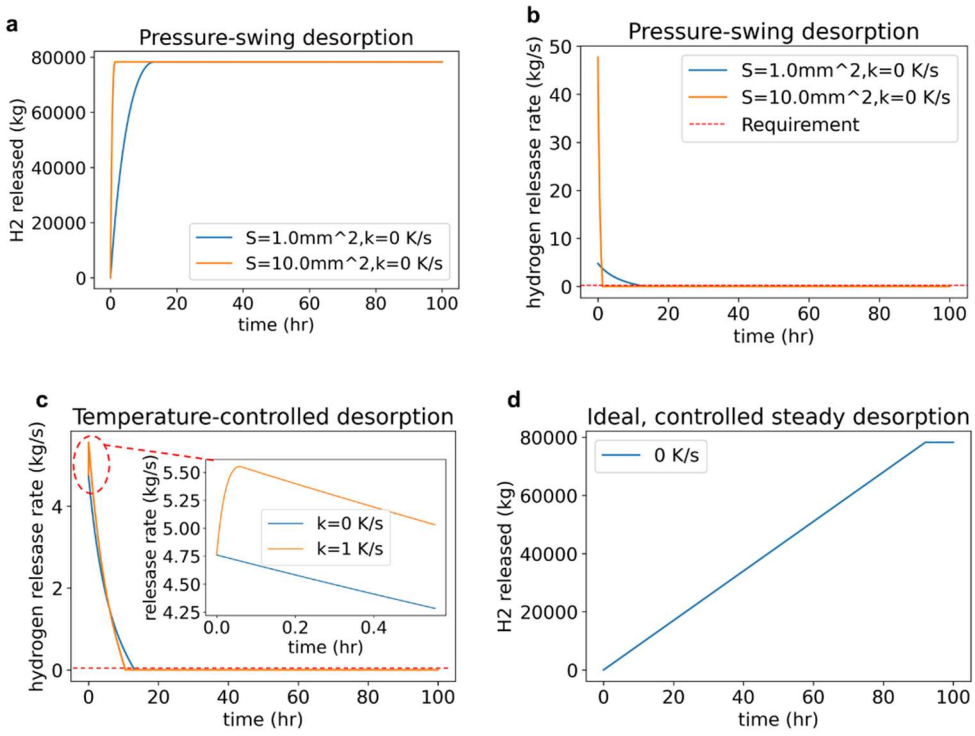

Supplementary Figure 8 | Representative examples of the modeled hydrogen desorption behavior under different release patterns. **a**, The total amount of hydrogen released during pressure-swing desorption. **b**, modeled hydrogen release rate during pressure-swing desorption. **c**, Comparison between temperature-swing desorption (orange) and pressure-swing desorption (blue). **d**, The ideal controlled release of hydrogen used for the TEA in this study.

Note 8 Compressed H_2 storage and liquid hydrogen storage

In this study, both the system-level performance and TEA for the compressed hydrogen storage is modeled using the same methodology as described in Supplementary Notes 1 and 2, without the MOF contents. For example, Equation (4) is not used, and the amount of hydrogen stored per tank is calculated solely from the hydrogen density at the corresponding temperature and pressure. The thermodynamic properties of hydrogen are obtained under the desired temperature and pressure conditions for these two scenarios.

For compressed hydrogen gas storage under 170 bar and 350 bar, another modification made to the model is that the type of storage tank is changed from Type I to Type IV, which is suitable for the high pressure conditions. Type I tanks are used for compresssed hydrogen gas storage under 170 bar conditions. As seen from Supplementary Fig. 9, the system-level energy density of compressed hydrogen storage increased at lower temperatures. However, the increased hydrogen density does not compensate for the additional costs to store compressed hydrogen gas under lower temperature conditions. Therefore, for the compressed hydrogen gas storage modeled in this study, the LCOS increases at lower temperatures.

LH_2 is modelled under the temperature of 19 K and atmospheric pressure. Because the model is derived using an energy balance approach and the kinetic and potential energy terms are neglected, the pump used to transport the cooled hydrogen to the storage tank is not modelled. Also note that for both compressed hydrogen gas storage under low temperature conditions and LH_2, there are additional heat losses under low temperature due to heat transfer between ambient, which is not modelled in this study. Combining these

assumptions, the results in this study for LH_2 is a relatively optimum. In other words, the actual cost of LH_2 storage and compressed gas storage should be higher than the results demonstrated in this study.

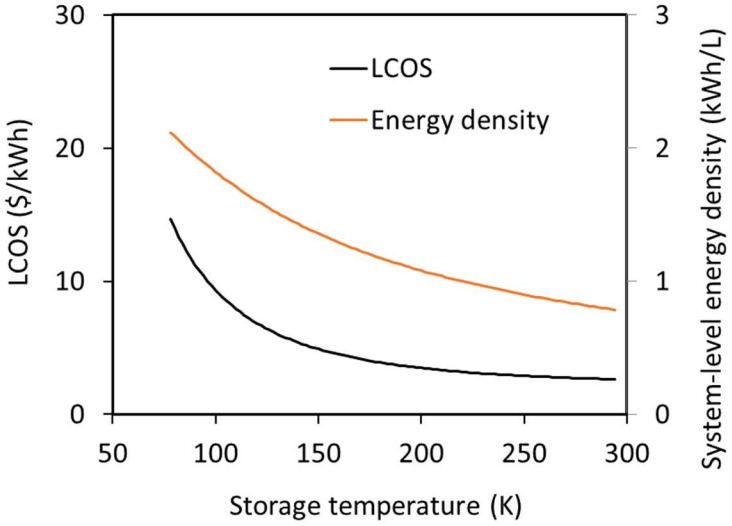

Supplementary Figure 9 | Levelized cost of storage and system-level energy density of compressed hydrogen gas storage at 350 bar.

Note 9 Discussions for extended temperature and pressure storage

Results shown in Fig. 2 in the main text shows that the within the modelled temperature range under near-ambient conditions (>200 K), the LCOS decreases at lower temperature while the system-level energy density increases. Although 223 K was selected as the lower limit for this analysis to avoid system complexity shown associated with cryogenic storage, it is beneficial to understand how LCOS and system-level energy density of the promising MOFs will change under temperatures lower that 223 K. Therefore, cost performance under extended temperature range is plotted in Supplementary Fig. 10 for two representative MOFs.

Shown in Supplementary Fig. 10a, Ni_2(*m*-dobdc) has higher excess uptake under near-ambient temperatures (200 K to 293 K), while MOF-5 has higher excess uptake under cryogenic conditions (below 150 K), and is commonly used in recent reports as promising storage candidate for cryogenic conditions[47,48]. For MOF-5, experimental data from literature[49] is used for low temperature conditions, which shows good agreement with the simulated excess uptake data from this study under near-ambient conditions (Supplementary Fig. 10a). Excess uptakes for Ni_2(*m*-dobdc) are extrapolated using the isotherms shown in Supplementary Fig. 7. Although these isotherms are fitted using experimental data above 200 K, the fitting agreements shows close match with experimental data from external collaborators under cryogenic conditions as low as 77 K. Thus can be used for this analysis under 150 K.

Supplementary Fig. 10b and Supplementary Fig. 10c show that for both MOFs, the system-level energy density increases under low temperature conditions, but accompanies with higher LCOS, mainly due to the dramatic increase of refrigeration costs discussed in Supplementary Note 2 and Supplementary Fig. 3. In terms of cost, the optimal cost range is slightly below ambient conditions, approximately the 200K to

233 K range for all conditions, except for MOF-5 under 0.2 bed and pellet porosity, which is lower (200K to 125 K shown in Supplementary Fig. 10c). Note that for cryogenic conditions, both in laboratory and industrial applications, significantly more complex refrigeration systems are required than near-ambient conditions around 223 K, on top of higher costs.[20,22,50] Therefore, the tradeoff between cost and energy density should be analyzed according to specific applications, for example space limitation and tolerance for additional complexity.

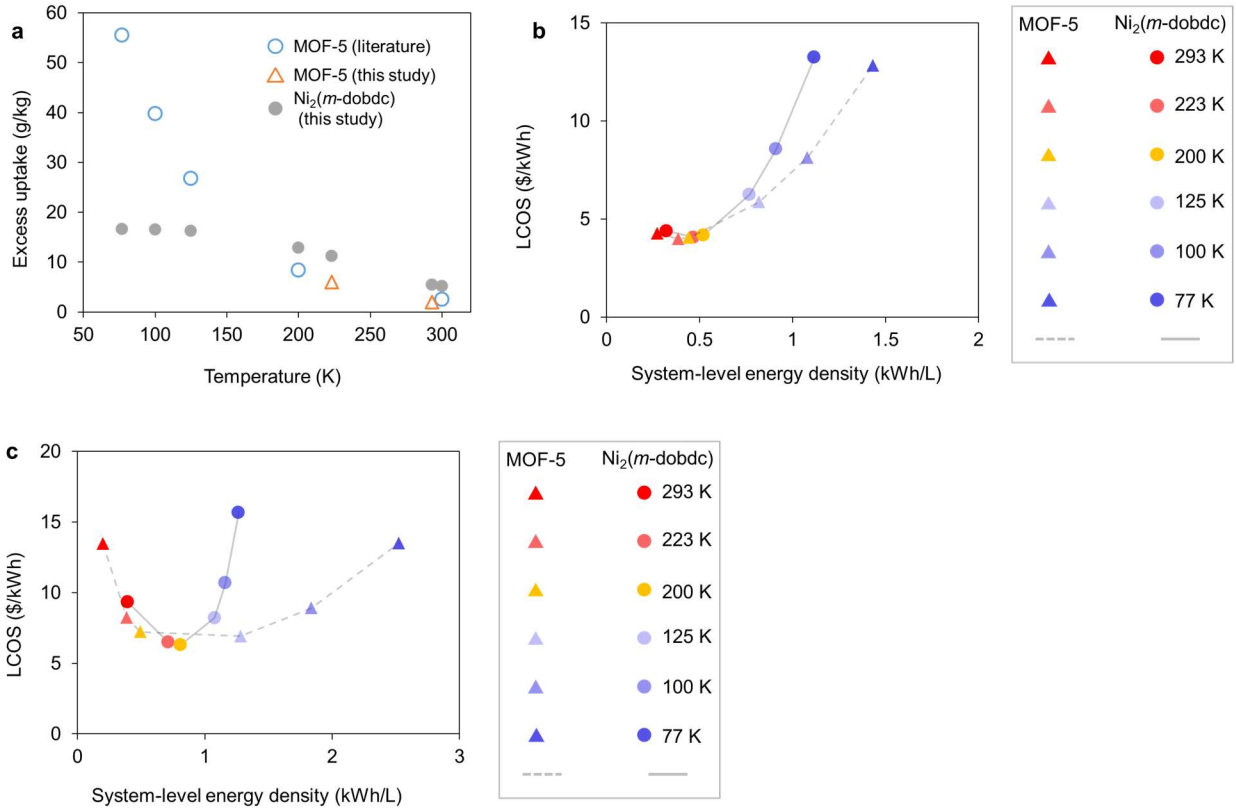

Supplementary Figure 10 | Additional performance results for extended temperature range (293K-77K, 90 bar) of selected MOFs. a, Excess uptake data used under extended temperature range, literature data for MOF-5 extracted from Purewal et al. 2012[49]. **b,** LCOS and system-level energy density for Ni_2(m-dobdc) and MOF-5 from 293 K to 77 K (90 bar, 0.6 bed and pellet porosities). **c,** LCOS and system-level energy density for Ni_2(*m*-dobdc) and MOF-5 from 293 K to 77 K (90 bar, 0.2 bed and pellet porosities).

For pressure, the increased energy density is the main benefit of pressurizing from 100 bar, the recommended large-scale above-ground storage pressure[51], to 170 bar, with relative less decrease in LCOS. Quantitatively, under 0.2 packing porosity, the increase in energy density from 100 bar (or 90 bar as analyzed in Fig. 2 of the main text) to 170 bar is approximately 30%, while the reduction of LCOS is only around 8%. As discussed in the Methods Section of the main text, the 100-bar recommendation for above-ground storage is set to avoid complexations of storage tanks[51]. In some cases (i.e., space limitation) the storage pressure can be moderately increased between 100 to 170 bar to stay within the limit of Type I storage tanks to reduce the footprint required[5,52-55].

Storing at higher pressure ranges (i.e., up to 350 bar) will no doubt increase the system-level energy density, but will require type IV storage tanks, which is considerably more expensive than Type I tanks

(Supplementary Note 2). Moreover, higher pressure would require significantly more complex storage infrastructure other than storage tank, such as distributing the hydrogen to the fuel cells[52].

Most importantly, the pressure range is well-above the experimental pressures for most of the MOFs studied. Thus, not only limited amount of experimental data on the candidate MOFs are available to validate the uptakes, not enough data has shown the effect of such high pressure to the durability and adsorption mechanisms of MOFs. Due to the above-mentioned considerations, higher pressure storage conditions are not modelled, and 100 bar–170 bar storage is recommended, and the detailed selection should depend on the specific applications.

Note 10 LCOS analysis for regular back-up and load optimization scenarios

Supplementary Fig. 11 shows the LCOS and system-level energy density when the system is used only to cover regular outage in the U.S.[56-58], which requires one charge/discharge cycle per year. As discussed in the main text, this application is relatively expensive among the scenarios depicted in Fig. 2e of the main text, which might only be consider by end-users such as data centers that is able to dedicate large portions of their power expenditure to back-up systems.[59]

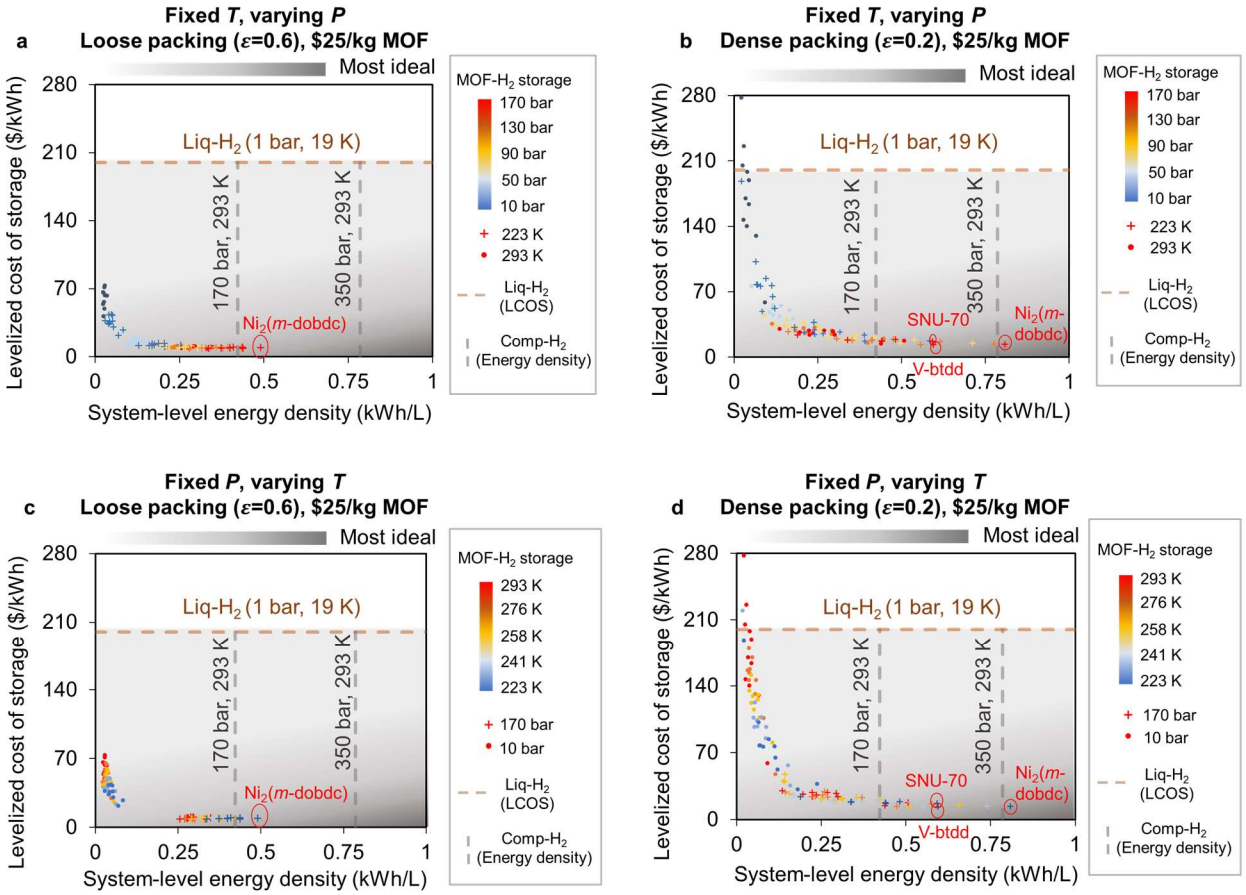

Supplementary Figure 11 | Performance of promising MOFs compared with conventional physical storage methods under 96-hour annual storage duration. The following caption is the same as Fig. 2 (a to d) in the main text. **a** and **b**, Fixed temperature under different pressures. **c** and **d**, Fixed pressure under different temperatures. **a** and **c**, Loose packing conditions at 0.6 bed and pellet porosities (ε=0.6). **b** and **d**, Dense packing conditions at 0.2 bed and pallet porosities (ε=0.2, 80% filled with MOF). Costs are

reported as installed cost. LCOS is for back-up power scenario (operational parameters listed in Table 2 of the main text). System-level energy density for Liq-H_2 in this analysis is 2.4 kWh/L.

Supplementary Fig. 12 shows the results for an extended application scenario (1440 hours), which can be used for more load optimization-focused application, for example up to 4 hours daily peak shaving for 350 days and 60-70 hours of regular back-up per year. As mentioned in the main text, the detailed operating pattern is highly geographical-dependent[60], and will benefit from market analysis that takes facility revenue into consideration.

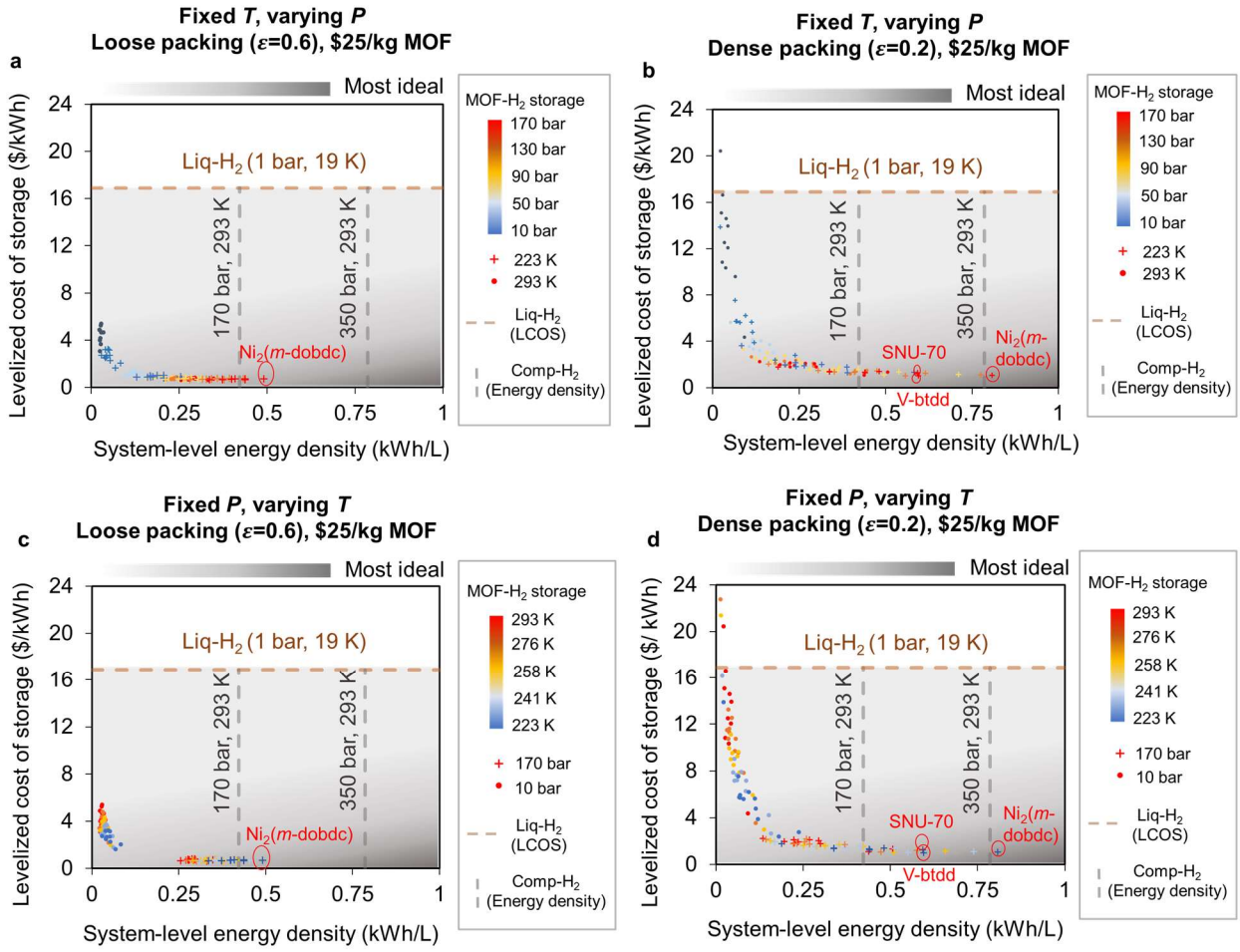

Supplementary Figure 12 | Performance of promising MOFs compared with conventional physical storage methods under 1440-hour annual storage duration. The following caption is the same as Fig. 2 (a to d) in the main text. **a** and **b**, Fixed temperature under different pressures. **c** and **d**, Fixed pressure under different temperatures. **a** and **c**, Loose packing conditions at 0.6 bed and pellet porosities (ε=0.6). **b** and **d**, Dense packing conditions at 0.2 bed and pallet porosities (ε=0.2, 80% filled with MOF). Costs are reported as installed cost. LCOS is for back-up power scenario (operational parameters listed in Table 2 of the main text). System-level energy density for Liq-H_2 in this analysis is 2.4 kWh/L.

Note 11 Cost estimates for electrolyzers, fuel cells, batteries, PSH, and Generators

Supplementary Table 7 summarizes the critical information used to determine the cost of electrolyzers and fuel cells. Based on previous literature, the efficiency for the commercialized alkaline water electrolyzer is in the range of 59% to 70%, and the efficiency of the near-commercialized and commercialized proton exchange membrane (PEM) electrolyzers are 60%–80%.[61-63] Therefore, a conservative value of 60% is used in this study to calculate the cost of the upstream electrolyzers.

Supplementary Table 7 | Key assumptions for integrating the MOF H_2 storage system with fuel cells and electrolyzers

Value	Value	Ref
Electrolyzer efficiency	60%	Chi and Yu, 2018[61]; Kumar and Himabindu, 2019[62]; Esposito, 2017[63]
Storage and fuel cell efficiency	35%	Barbir 2005[64]; Barbir, 2009[65]; Wei et al., 2014[66]; and this study
Grid integration	$18/kW	Mongird et al., 2020[25]
Additional installation costs for storage unit ("included in others in Fig. 4b of main text")	25% of storage CAPEX	This study

For the capital costs in terms of $/kW (electrolyzer requirement), we extrapolate the representative capital cost and log10 electrolyzer sizes (kW) from Yates et al. 2020,[67] which reviewed and summarized the cost contemporary published costs and sizes of electrolyzers. Supplementary Fig. 13 shows the key data used for the linear interpolation suitable for the size range required in this study. For the electrolyzer, the uncertainty range in Fig. 4a and Fig. 4b of the main text was estimated based on the Monte Carlo simulation performed by Yates et al. 2020,[67] which was approximately 30% for the lower bound and 50% for the higher bound. The electrolyzer cost estimated by PNNL's Grid Energy Storage Technology Cost and Performance Assessment report[25] also falls within approximately the 50% markup limit. Note that the power used to estimate the electrolyzer cost is the power input requirement of the electrolyzer, rather than the output power, because the feed parameter to the Monte Carlo simulation[67] is the nominal power. The efficiencies are another factor that leads to the high cost of electrolyzer in this study, expecially in fast charge scenarios. For example, if a 10 MW back-up power system designed for 96-hour storage is targetted to be charged in 48 hours, the corresponding electrolyzer power would need to be approximately 95 MW accounting for the energy losses in electrolyzer output, storage, and fuel cells, etc.

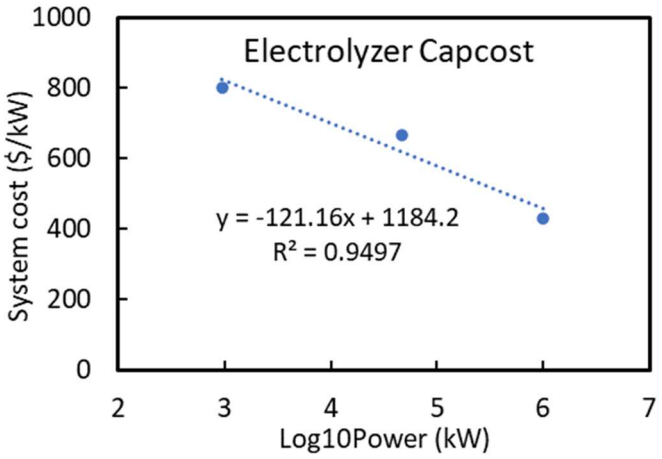

Supplementary Figure 13 | Representative electrolyzer system cost vs. size (kW) relationship. The extrapolation covers approximately the average values from the contemporary published cost analyses. Data extracted from refs,[68-70] which was previously reported and summarized by Yates et al. 2020.[67]

For the fuel cell, we assume $200/kWe output of direct manufacturing cost[66].To account for the uncertainties, 50% markup is added to the electrolyzer and fuel cell cost for the upper bound of the error costs in Fig. 4a and Fig. 4b in the main text, also to account for the potential corporate markups. 30% markdown is added as the lower bound, which for the electrolyzers are approximately the range reported in Yates et al. 2020[67]. The resulting capital cost of electrolyzer is then normalized to 10 MW output system for the back-up power.

The system costs range of batteries and pumped storage hydropower (PSH) are estimated from PNNL's Grid Energy Storage Technology Cost and Performance Assessment report.[25] For batteries, the system cost for storage capacity from 2 to 10 hours is extracted from Appendix 3 of the report.[25] Since the given system cost increases linearly with the storage capacity, a linear interpolation is performed to obtain the system costs beyond 10 hours in Fig. 4 and Fig. 5 in the main text. The lower bound and higher bound of the battery costs are set using the most economical and expensive costs between lithium-ion, lead acid, and vanadium redox flow batteries. A similar methodology is used to predict the cost range for PSH using the two storage capacities (4 and 10 h) for 100 MW in Figure #7 of the referenced report.[25] Note that for PSH, 100 MW is used in the report, so the value for 10 MW systems should be slightly higher than what is used in this study.

For diesel and natural gas generators, the reported capital costs for the diesel and natural gas generators are in the range of 800 and1000 $/kWh, respectively[57]. National average of diesel and natural gas costs used in this study are 19.5 $/MBTU and 8 $/MTU, respectively including delivery to the end-user[57]. Using the 9 kWh/L energy density, the cost of the storage tank for diesel (<1% of total capital), and its change (0.1% of total capital) from 10 MWh to 1000 MWh is determined negligible compared with the capital and fuel cost[20,71]. Natural gas is assumed to be supplied using pipeline and included in the fuel cost.

Supplementary references

1 Thornton, M. J. & Simpson, L. J. *System Design, Analysis, and Modeling Activities Supporting the DOE Hydrogen Storage Engineering Center of Excellence (HSECoE): Final Project Report*. (National Renewable Energy Laboratory, 2019).

2 Tamburello, D. *et al.* in *ASME Power Conference* (2018).

3 Brooks, K. P. *et al. PNNL Development and Analysis of Material-Based Hydrogen Storage Systems for the Hydrogen Storage Engineering Center of Excellence*. (Pacific Northwest National Laboratory, 2016).

4 Ramirez-Vidal, P. *et al.* A step forward in understanding the hydrogen adsorption and compression on activated carbons. *ACS Applied Materials & Interfaces* **13**, 12562-12574 (2021).
5 Ahmed, A. *et al.* Exceptional hydrogen storage achieved by screening nearly half a million metal-organic frameworks. *Nature communications* **10**, 1-9 (2019).
6 Bobbitt, N. S., Chen, J. & Snurr, R. Q. High-throughput screening of metal–organic frameworks for hydrogen storage at cryogenic temperature. *The Journal of Physical Chemistry C* **120**, 27328-27341 (2016).
7 Goldsmith, J., Wong-Foy, A. G., Cafarella, M. J. & Siegel, D. J. Theoretical limits of hydrogen storage in metal–organic frameworks: opportunities and trade-offs. *Chemistry of Materials* **25**, 3373-3382 (2013).
8 García-Holley, P. *et al.* Benchmark study of hydrogen storage in metal–organic frameworks under temperature and pressure swing conditions. *ACS Energy Letters* **3**, 748-754 (2018).
9 Bucior, B. J. *et al.* Energy-based descriptors to rapidly predict hydrogen storage in metal–organic frameworks. *Molecular Systems Design & Engineering* **4**, 162-174 (2019).
10 Fairen-Jimenez, D. *et al.* Understanding excess uptake maxima for hydrogen adsorption isotherms in frameworks with rht topology. *Chemical Communications* **48**, 10496-10498 (2012).
11 Dubbeldam, D., Calero, S., Ellis, D. E. & Snurr, R. Q. RASPA: molecular simulation software for adsorption and diffusion in flexible nanoporous materials. *Molecular Simulation* **42**, 81-101 (2016).
12 Groom, C. R., Bruno, I. J., Lightfoot, M. P. & Ward, S. C. The Cambridge structural database. *Acta Crystallographica Section B: Structural Science, Crystal Engineering and Materials* **72**, 171-179 (2016).
13 Klymyshyn N.A. *PNNL Tank Mass Estimator for Cross Comparison of Type 1, Type 3, and Type 4 Pressure Vessels ("Tankinator")*, (Pacific Northwest National Laboratory, 2013).
14 *"Department of Energy (DOE) Technical Targets for Onboard Hydrogen Storage for Light-Duty Vehicles"*), https://www.energy.gov/eere/fuelcells/doe-technical-targets-onboard-hydrogen-storage-light-duty-vehicles.
15 Bell, I. H., Wronski, J., Quoilin, S. & Lemort, V. Pure and pseudo-pure fluid thermophysical property evaluation and the open-source thermophysical property library CoolProp. *Industrial & engineering chemistry research* **53**, 2498-2508 (2014).
16 Zhao, R. *et al.* Performance analysis of temperature swing adsorption for CO2 capture using thermodynamic properties of adsorbed phase. *Applied Thermal Engineering* **123**, 205-215 (2017).
17 Jiang, L. *et al.* Comparative analysis on temperature swing adsorption cycle for carbon capture by using internal heat/mass recovery. *Applied Thermal Engineering* **169**, 114973 (2020).
18 Geankoplis, C. J. *Transport processes and separation process principles:(includes unit operations)* (Prentice Hall Professional Technical Reference, 2003).
19 Dicks, A. L. & Rand, D. A. J. in *Fuel Cell Systems Explained* 351-399 (Wiley, 2018).
20 Turton, R., Bailie, R. C., Whiting, W. B. & Shaeiwitz, J. A. *Analysis, synthesis and design of chemical processes* 5th Edition (Pearson Education, 2018).
21 Anastasopoulou, A. *et al.* Technoeconomic analysis of metal–organic frameworks for bulk hydrogen transportation. *Energy & Environmental Science* **14**, 1083-1094 (2021).
22 Luyben, W. L. Estimating refrigeration costs at cryogenic temperatures. *Computers & Chemical Engineering* **103**, 144-150 (2017).
23 *2020 Annual Technology Baseline*, (National Renewable Energy Laboratory, 2020), https://atb.nrel.gov/.
24 *Standard for Emergency and Standby Power Systems*, (National Fire Protection Association, 2022), https://www.nfpa.org/codes-and-standards/all-codes-and-standards/list-of-codes-and-standards/detail?code=110.

25 Mongird, K. *et al. 2020 Grid Energy Storage Technology Cost and Performance Assessment*. (Pacific Northwest National Laboratory, 2020).
26 Tao, L., Milbrandt, A., Zhang, Y. & Wang, W.-C. Techno-economic and resource analysis of hydroprocessed renewable jet fuel. *Biotechnology for Biofuels* **10**, 261 (2017).
27 Parks, G. *Hydrogen station compression, storage, and dispensing technical status and costs*. (National Renewable Energy Laboratory, 2014).
28 *Wholesale Electricity and Natural Gas Market Data*, (U.S. Energy Information Administration, 2021), https://www.eia.gov/electricity/wholesale/.
29 El-Sayed, E.-S. M. & Yuan, D. Waste to MOFs: sustainable linker, metal, and solvent sources for value-added MOF synthesis and applications. *Green Chemistry* **22**, 4082-4104 (2020).
30 DeSantis, D. *et al.* Techno-economic analysis of metal–organic frameworks for hydrogen and natural gas storage. *Energy & Fuels* **31**, 2024-2032 (2017).
31 *Compensation costs in private industry averaged $36.23 per hour worked in December 2020*, (U.S. Department of Labor, 2021). https://www.bls.gov/opub/ted/2021/compensation-costs-in-private-industry-averaged-36-23-per-hour-worked-in-december-2020.htm.
32 Jenkins, S. *CEPCI Archives*. (Chemical Engineering, 2020).
33 Spurgeon, J. M. & Kumar, B. A comparative technoeconomic analysis of pathways for commercial electrochemical CO 2 reduction to liquid products. *Energy & Environmental Science* **11**, 1536-1551 (2018).
34 Shaner, M. R., Atwater, H. A., Lewis, N. S. & McFarland, E. W. A comparative technoeconomic analysis of renewable hydrogen production using solar energy. *Energy & Environmental Science* **9**, 2354-2371 (2016).
35 James, B., Colella, W., Moton, J., Saur, G. & Ramsden, T. *PEM electrolysis H2A production case study documentation*. (National Renewable Energy Laboratory, 2013).
36 Colella, W. G., James, B. D., Moton, J. M., Saur, G. & Ramsden, T. in *Electrolytic hydrogen production workshop, NREL, Golden, Colorado*).
37 Carvill, J. *Mechanical engineer's data handbook* (Butterworth-Heinemann, 1994).
38 Lakatos, Á. & Kovács, Z. Comparison of thermal insulation performance of vacuum insulation panels with EPS protection layers measured with different methods. *Energy and Buildings* **236**, 110771 (2021).
39 Geng, Y., Han, X., Zhang, H. & Shi, L. Optimization and cost analysis of thickness of vacuum insulation panel for structural insulating panel buildings in cold climates. *Journal of Building Engineering* **33**, 101853 (2021).
40 Ahluwalia, R. K. *et al.* Technical assessment of cryo-compressed hydrogen storage tank systems for automotive applications. *International Journal of Hydrogen Energy* **35**, 4171-4184 (2010).
41 Bigelow, E. & Lewis, M. *Conformable Hydrogen Storage Pressure Vessel*. (Center for Transportation and the Environment, 2018).
42 James, B., Houchins, C., Huya-Kouadio, J. & DeSantis, D. *Final Report: Hydrogen Storage System Cost Analysis*. (Strategic Analysis, 2016).
43 Wieme, J. *et al.* Thermal Engineering of Metal–Organic Frameworks for Adsorption Applications: A Molecular Simulation Perspective. *ACS applied materials & interfaces* **11**, 38697-38707 (2019).
44 Kapelewski, M. T. *et al.* M2 (m-dobdc)(M= Mg, Mn, Fe, Co, Ni) metal–organic frameworks exhibiting increased charge density and enhanced H2 binding at the open metal sites. *Journal of the American Chemical Society* **136**, 12119-12129 (2014).

45 Cherrad, N., Selloum, D. & Tingry, S. Modeling the control of the desorption rate of hydrogen released from the adsorption storage bed to supply a fuel cell. *International Journal of Hydrogen Energy* **45**, 17605-17612 (2020).
46 Richard, M.-A., Bénard, P. & Chahine, R. Gas adsorption process in activated carbon over a wide temperature range above the critical point. Part 1: modified Dubinin-Astakhov model. *Adsorption* **15**, 43-51 (2009).
47 Suresh, K. *et al.* Optimizing Hydrogen Storage in MOFs through Engineering of Crystal Morphology and Control of Crystal Size. *Journal of the American Chemical Society* **143**, 10727-10734 (2021).
48 Palla, S. & Kaisare, N. S. Evaluating the impact of pellet densification and graphite addition for design of on-board hydrogen storage in a fixed bed of MOF-5 pellets. *International Journal of Hydrogen Energy* **45**, 25875-25889 (2020).
49 Purewal, J. *et al.* Improved Hydrogen Storage and Thermal Conductivity in High-Density MOF-5 Composites. *The Journal of Physical Chemistry C* **116**, 20199-20212 (2012).
50 Ladner, D. R. in *International Cryocooler Conference Inc.* 633-644 (2011).
51 Andersson, J. & Grönkvist, S. Large-scale storage of hydrogen. *International journal of hydrogen energy* **44**, 11901-11919 (2019).
52 Rivard, E., Trudeau, M. & Zaghib, K. Hydrogen storage for mobility: a review. *Materials* **12**, 1973 (2019).
53 Wang, H., Leung, D. Y., Leung, M. & Ni, M. A review on hydrogen production using aluminum and aluminum alloys. *Renewable and sustainable energy reviews* **13**, 845-853 (2009).
54 Barthélémy, H., Weber, M. & Barbier, F. Hydrogen storage: recent improvements and industrial perspectives. *International Journal of Hydrogen Energy* **42**, 7254-7262 (2017).
55 Shet, S. P., Shanmuga Priya, S., Sudhakar, K. & Tahir, M. A review on current trends in potential use of metal-organic framework for hydrogen storage. *International Journal of Hydrogen Energy* **46**, 11782-11803 (2021).
56 Stone, B. *et al.* Compound climate and infrastructure events: How electrical grid failure alters heat wave risk. *Environmental Science & Technology* **55**, 6957-6964 (2021).
57 Ericson, S. J. & Olis, D. R. *A comparison of fuel choice for backup generators*. (National Renewable Energy Laboratory, 2019).
58 *Annual Electric Power Industry Report*, (U.S. Energy Information Administration, 2021), https://www.eia.gov/electricity/data/eia861/
59 Yin, Y. *et al.* COPA: Highly Cost-Effective Power Back-Up for Green Datacenters. *IEEE Transactions on Parallel and Distributed Systems* **31**, 967-980 (2020).
60 Heptonstall, P. J. & Gross, R. J. K. A systematic review of the costs and impacts of integrating variable renewables into power grids. *Nature Energy* **6**, 72-83 (2021).
61 Chi, J. & Yu, H. Water electrolysis based on renewable energy for hydrogen production. *Chinese Journal of Catalysis* **39**, 390-394 (2018).
62 Kumar, S. S. & Himabindu, V. Hydrogen production by PEM water electrolysis–A review. *Materials Science for Energy Technologies* **2**, 442-454 (2019).
63 Esposito, D. V. Membraneless electrolyzers for low-cost hydrogen production in a renewable energy future. *Joule* **1**, 651-658 (2017).
64 Barbir, F. in *PEM Fuel Cells* 33-72 (Academic Press, 2005).
65 Barbir, F. in *Encyclopedia of Electrochemical Power Sources* 224-237 (Elsevier, 2009).
66 Wei, M. *et al. A total cost of ownership model for low temperature PEM fuel cells in combined heat and power and backup power applications*. (Lawrence Berkeley National Laboratory, 2014).

67 Yates, J. *et al.* Techno-economic Analysis of Hydrogen Electrolysis from Off-Grid Stand-Alone Photovoltaics Incorporating Uncertainty Analysis. *Cell Reports Physical Science* **1**, 100209 (2020).
68 Parra, D. & Patel, M. K. Techno-economic implications of the electrolyser technology and size for power-to-gas systems. *International Journal of Hydrogen Energy* **41**, 3748-3761 (2016).
69 Hinkley, J. *et al. Cost assessment of hydrogen production from PV and electrolysis*. (Commonwealth Scientific and Industrial Research Organisation, 2016).
70 *The Future of Hydrogen*, (International Energy Agency 2019), https://www.iea.org/reports/the-future-of-hydrogen
71 De Jong, E. & Gruter, G.-J. in *SAE 2009 Powertrains Fuels and Lubricants Meeting* (2009).